Oxygen Vacancy Induced Bismuth Oxyiodide with Remarkably Increased Visible-Light Absorption and Superior Photocatalytic Performance

Yongchao Huang, Haibo Li, Muhammad-Sadeeq Balogun, Wenyue Liu, Yexiang Tong, Xihong Lu,* and Hongbing Ji*

Department of Chemical Engineering, MOE of the Key Laboratory of Bioinorganic and Synthetic Chemistry, School of Chemistry and Chemical Engineering, The Key Lab of Low-Carbon Chemistry & Energy Conservation of Guangdong Province, Sun Yat-Sen University, Guangzhou 510275, People's Republic of China

S *Supporting Information*

ABSTRACT: With the increasingly serious environmental problems, photocatalysis has recently attracted a great deal of attention, with particular focus on water and air purification and disinfection. Herein, we show an electroreduction strategy to improve significantly the solar absorption and donor density of BiOI nanosheet photocatalyst by introducing oxygen vacancies. These oxygen-deficient BiOI nanosheets exhibit an unexpected red shift of about 100 nm in light absorption band and 1 order of magnitude improvement in donor density compared to the untreated BiOI nanosheets and show 10 times higher photocatalytic activity than the untreated BiOI nanosheets for methyl orange (MO) degradation under visible light irradiation. Moreover, the as-prepared oxygen-deficient BiOI nanosheets also have excellent cycling stability and superior photocatalytic performance toward other dye pollutants.

KEYWORDS: bismuth oxyhalide, oxygen vacancy, visible light, photocatalytic
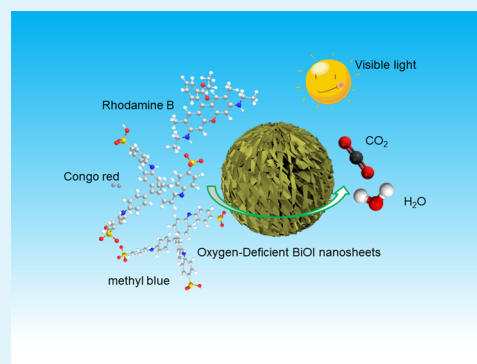
1. INTRODUCTION

Semiconductor-based photocatalysts have attracted tremendous attention in recent years for their abundant applications in solar energy conversion and environmental remediation.[1−6] Transition metal oxides with wide band gap such as TiO_2,[7−9] ZnO,[10] SnO_2,[11] and WO_3[12,13] have been employed extensively as photocatalysts due to their low cost and high chemical stability. However, most of these photocatalysts are only capable of utilizing the ultraviolet light (about 4% of the solar energy) and/or a very small quantity of visible light due to their wide band gaps, which greatly limit their photocatalytic performance and hinder their practical applications. To maximize the utilization of the solar energy, numerous efforts have been paid to exploring visible-light-driven photocatalysts, and plentiful impressive photocatalysts with good photocatalytic activity have been developed. Among them, bismuth oxyiodide (BiOI) is emerging as one of the most attractive visible-light-driven photocatalysts due to its small band gap of 1.6−1.9 eV and unique structure.[14−23] It possesses an open, layered crystal structure consisting of $[Bi_2O_2]^{2+}$ layers sandwiched between two slabs of halogen ions (Scheme 1). The interleaved layer structure between positive $[Bi_2O_2]^{2+}$ slabs and negative iodide slabs builds spontaneously internal static electric fields, which can induce the effective separation of photogenerated electron−hole pairs.[19,24−29] Nevertheless, the reported photocatalytic efficiencies of BiOI are notoriously low for practical

Scheme 1. Schematic Representation of the Crystal Structure of BiOI. (a) Three-Dimensional Projection. (b, c) $[Bi_2O_2]^{2+}$ Layers along with the $[010]$ and $[001]$ Direction, Respectively
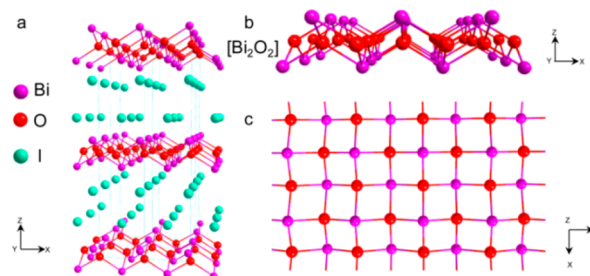
application owing to its poor conductivity and quick recombination rate of photogenerated charge carriers.

In recent years, intensive attempts have been dedicated to increase the photocatalytic activity of BiOI photocatalysts, and some strategies such as material structural designing,[16,19] noble metal decorating,[18,30−32] elemental doping,[14] and heterojunction[17,33−35] have been reported. For instance, the construction
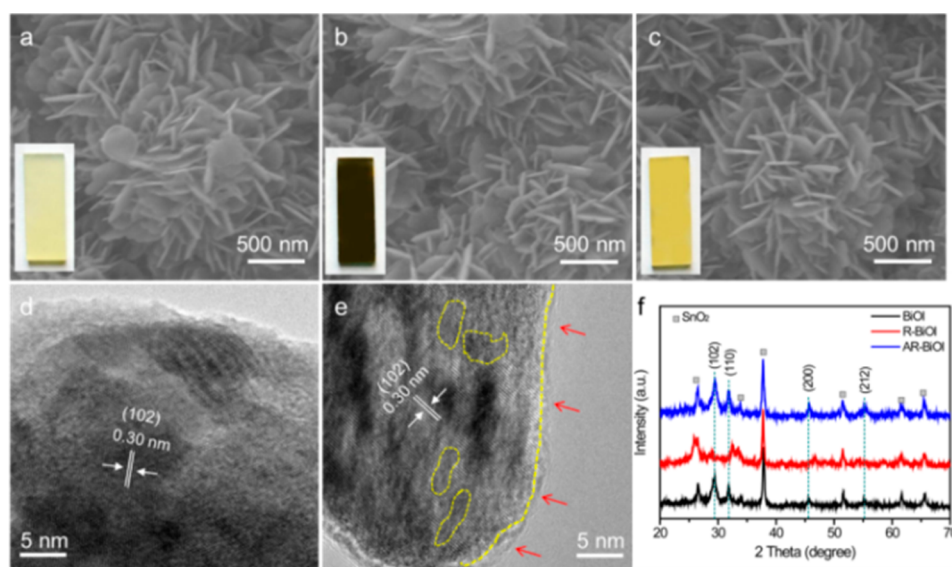
Figure 1. SEM images and photographs (lower insets) of (a) as-prepared BiOI nanosheets, (b) R-BiOI nanosheets, and (c) AR-BiOI nanosheets. HRTEM images of (d) as-prepared BiOI nanosheets and (e) AR-BiOI nanosheets. (f) XRD spectra collected for as-prepared BiOI, R-BiOI, and AR-BiOI samples.

of BiOI-based heterostructured composites with suitable banding alignment can greatly facilitate the separation of photogenerated electron−hole pairs and suppress their recombination, and hence enhance the photocatalytic activity of BiOI. In this respect, plentiful BiOI-based heterojunction photocatalysts such as BiOI/BiOBr,[17] BiOI/BiOCl,[33] BiOI/TiO$_2$,[36] BiOI/ZnWO$_4$,[35] BiOI/Bi$_2$S$_3$,[20] BiOI/ZnO,[34] and BiOI/AgI[30] have been widely developed and exhibited enhanced photoactivity. In addition, decorating noble metals such as Au,[32] Pt,[31] and Ag[18] have also proven to significantly improve the photocatalytic performance of BiOI due to the improvement of the charge separation and/or light-harvesting ability results from their surface plasmon resonance (SPR) property. However, the use of scarce and expensive noble metals leads to high cost, which severely hinders their practical application as photocatalysts. On the other hand, these strategies mentioned above do not change and/or improve the intrinsic properties of BiOI such as optical absorption property and charge transfer ability. It is highly desirable to intrinsically improve the photoactivity of the BiOI photocatalysts with an environmentally friendly and cost-effective method.

Oxygen vacancy is a fundamental and intrinsic defect in metal oxide semiconductors and has a critical effect on their electronic and physicochemical properties such as electronic band structures and optical absorption.[37−40] Recent reports have shown that the intrinsic metal oxide photocatalysts with oxygen vacancies can absorb visible light and display excellent visible light photocatalytic activity.[41−44] In view of the density functional theory (DFT) calculation on the electronic structure of BiOI, the top of the valence band (VB) is mainly dominated by both O$_{2p}$ and I$_{5p}$ orbits, whereas the bottom of the conduction band (CB) is mainly composed of Bi$_{6s}$ and Bi$_{6p}$ orbits.[14] Previously reported simulation results predicted that a new electronic state peak of Bi 6p state will be formed in the forbidden band of BiOX (X = Cl, Br, I) due to the existence of oxygen vacancies, which would be more beneficial for utilizing solar light.[40,45,46] Moreover, these oxygen vacancies could act as electron scavengers delaying electron−hole pair recombination

during the photoreaction process, thus improving the separation efficiency of the photogenerated electrons and holes.[40] These features inspired us to improve the visible light absorption and photoactivity of BiOI by introducing oxygen vacancies into BiOI. In this study, we demonstrated for the first time that the light-harvesting ability and the separation efficiency of the photogenerated electrons and holes of BiOI nanosheets can be improved simultaneously and significantly through creating oxygen vacancies within the BiOI. Oxygen-deficient BiOI nanosheets were readily obtained by a facile cost-effective electrochemical reduce method and showed a remarkable red shift of about 100 nm in light absorption band and 1 order of magnitude improvement in donor density compared to those of untreated BiOI nanosheets. Benefiting from the substantially increased visible light absorption and donor density, the oxygen-deficient BiOI nanosheets exhibited 10 times higher photocatalytic activity than the untreated BiOI nanosheets for methyl orange (MO) degradation under visible light irradiation. Moreover, they also possess excellent photocatalytic activities for other dye pollutants such as methyl blue (MB), rhodamine B (RhB), Congo red (CR), acid orange II (AO II), and phenol, as well as outstanding cycling performance.

2. EXPERIMENTAL METHODS

Preparation of BiOI Nanosheets. All the reagents were of analytical grade and were used without further purification. Deionized water was used throughout the experiments. The BiOI nanosheets arrays were synthesized by a solvothermal process. In a typical procedure, 20 mL of methanol containing 1 mmol KI was added dropwise to 1 mmol Bi(NO$_3$)$_3$ dissolved in 20 mL of glycol. The solutions were mixed together and stirred for 2 h to get a clear solution. FTO substrate (2.8 × 4.8 cm), ultrasonically cleaned in acetone and ethanol for 10 min each, was placed in the solution at an angle against the wall of a 50.0 mL Teflon liner with the conductive side facing down. The solvothermal synthesis was conducted at 160 °C for 8 h in an electric oven. The final products were washed with anhydrous ethanol several times and then dried at 60 °C for 2 h. The as-prepared BiOI was then annealed in air/N$_2$ (1:1) atmosphere at a temperature of 350 °C for 2 h. The product obtained was denoted as D-BiOI. The electroreduction of BiOI (denoted as R-BiOI) was

obtained by applying a voltage of −1.2 V vs Ag/AgCl for 200 s at room temperature in a three-electrode cell with a platinum counter electrode. The as-prepared R-BiOI was then annealed in air/N_2 (1:1) atmosphere at a temperature of 350 °C for 2 h. The product obtained was denoted as AR-BiOI.

Materials Characterizations. The morphology, structure, and composition of the materials were characterized by field-emission SEM (FE-SEM, JSM-6330F), TEM (TEM, JEM2010-HR, 200 kV), XPS (XPS, ESCALab250, Thermo VG), and X-ray diffractometry (XRD, D8 ADVANCE). EPR tests were carried out in the X-band (9.45 GHz) with 5.00 G modulation amplitude and a magnetic field modulation of 100 kHz using a Bruker, A300-10-12 Bruker EPR spectrometer at 77 K. The optical properties of the products were measured with a UV−vis−NIR spectrophotometer (UV−vis−NIR, Shimadzu UV-2450). Room-temperature photoluminescence (PL) spectra were measured using a combined fluorescence lifetime and steady-state spectrometer (FLS920, EDINBURGH), and the exaction wavelength was 400 nm. Nitrogen adsorption/desorption isotherms at 77 K were conducted on an ASAP 2020 V3.03 H instrument. All samples (powders) were outgassed at 100 °C for 5 h under flowing nitrogen before measurements.

Electrochemical Measurements. The electrochemical measurements were carried out in a three-electrode cell. All the electrochemical measurements were performed on a CHI 760D electrochemical workstation at room temperature. The electrolyte is 0.1 M Na_2SO_4 solution.

Photocatalytic Activity Test. The photocatalytic measurements were carried out in a column container at ambient temperature (Supporting Information Figure S5). One sliver of FTO substrate (2.8 × 4.8 cm) covered with the as-prepared BiOI (15 mg) was inserted in the column container. The photoreactor was filled with 100.0 mL of 10.0 mg $L^{−1}$ MO. Prior to irradiation, the solution was magnetically stirred in the dark for 30 min to establish absorption−desorption equilibrium. The samples were evaluated by degradation of the dyes in an aqueous solution under a 500 W Xe lamp with a 420 nm UV light cut filter. The light intensity is 100 mW $cm^{−2}$. O_2 was bubbled into the photoreactor at a flow rate of 100.0 mL $min^{−1}$ to promote the formation of the active $•O^{2−}$ radicals. After UV light irradiation, 3.0 mL of the reactive solution was taken out at regular time intervals for measurement by UV−vis spectrophotometry. The same test for the MO was also carried out on methyl blue (MB), rhodamine B (RhB), Congo red (CR), acid orange II (AO II), and phenol.

3. RESULTS AND DISCUSSION

BiOI nanosheets were first grown on F-doped SnO_2 glass (FTO) substrate using a hydrothermal method reported elsewhere[47] (details in the Experimental Methods). As shown in inset of Figure 1a, a uniform pale yellow film was obtained on the FTO substrate after hydrothermal reaction. Typical scanning electron microscopy (SEM) images reveal that the FTO surface was covered uniformly by a large number of nanosheets (Figure 1a and Supporting Information Figure S1a). These nanosheets have a thickness of around 40 nm and width of 300 nm, respectively. To introduce oxygen vacancies into the BiOI nanosheets, the as-prepared BiOI nanosheets served as a working electrode and were electroreduced with a potential of −1.2 V vs Ag/AgCl for 200 s in 0.1 M Na_2SO_4 (denoted as R-BiOI), and then annealed at 350 °C in Air/N_2 (1:1) atmosphere (denoted as AR-BiOI). The color of BiOI film first changed from pale yellow to black after electroreduction (inset in Figure 1b), and then to deep yellow after calcination (inset in Figure 1c). However, SEM studies reveal that there is no obvious morphological change in nanosheet structure upon electroreduction and thermal treatment (Figure 1b, c and Supporting Information Figure S1). X-ray diffraction (XRD) spectra of untreated BiOI, R-BiOI, and AR-BiOI samples were collected to determine the crystal structure and possible phase

changes during electroreduction and annealing processes. As shown in Figure 1f, beside the diffraction peaks originating from FTO substrate, the peaks collected from untreated BiOI can be indexed as tetragonal BiOI (PCPDF no.: 10-0445). After electroreduction, these diffraction tetragonal BiOI peaks disappeared, suggesting that the phase of the R-BiOI has changed. To further investigate the microstructure of the BiOI nanosheets, transmission electron microscopy (TEM) studies were further performed. TEM and selected-area electron diffraction (SAED) analyses shows that the BiOI sample possesses hierarchical architectures that assembled by many high-crystalline nanosheets (Supporting Information Figure S1). A high-resolution TEM (HRTEM) image collected from the BiOI nanosheets reveals clear lattice fringes with a interplanar spacing of 0.30 nm, which is consistent with the d-spacing of (102) planes of tetragonal BiOI (Figure 1d). Figure 1e displays a typical HRTEM image of AR-BiOI nanosheets. Significantly, in comparison with untreated BiOI nanosheet, the surface and inside of AR-BiOI nanosheets became disordered (marked by yellow region and arrows), suggesting the generation of numerous oxygen vacancies after electroreduction and calcination.

To confirm that oxygen vacancies could be induced into BiOI through electroreduction and calcination, X-ray photoelectron spectroscopy (XPS) and electron paramagnetic resonance (EPR) analyses were performed. For better understanding, the as-prepared BiOI nanosheets were directly annealed at 350 °C in air/N_2 (1:1) atmosphere (denoted as D-BiOI). SEM and XRD analyses confirm that the morphology and phase of D-BiOI nanosheets are similar to those of untreated BiOI and AR-BiOI nanosheets (Supporting Information Figure S2). As shown in Supporting Information Figure S3a, the XPS survey spectra collected from untreated BiOI, R-BiOI, AR-BiOI, and D-BiOI samples are very similar. Carbon is believed to be incorporated during sample preparation and subsequent handling. This indicates that the electroreduction and calcination did not introduce impurities into the BiOI nanosheets. Supporting Information Figure S3b compares the core-level I 3d XPS spectra of untreated BiOI, R-BiOI, AR-BiOI, and D-BiOI samples. The peaks with binding energy of 618.9 and 630.4 eV are the characteristic I $3d_{5/2}$ and I $3d_{3/2}$ peaks of BiOI, respectively.[48] No any obvious shift and variation in the binding energy were observed for all the BiOI samples, revealing that the chemical states of I for all BiOI samples are almost the same. The upper of Figure 2a shows the core-level Bi XPS spectra of untreated BiOI, R-BiOI, and AR-BiOI samples. The binding energies of the Bi $4f_{7/2}$ and Bi $4f_{5/2}$ peaks of BiOI samples are located at 159.1 and 164.4 eV, which are consistent with the reported values for BiOI.[34] In comparison to untreated BiOI sample, the Bi 4f5/2 and Bi 4f7/2 peaks of R-BiOI sample exhibit a shift of about 0.3 eV toward lower binding energy, which is indicative of the presence of lower charge Bi ions in R-BiOI nanosheets.[38,44] This result clearly verifies that the Bi^{3+} ions can be reduced to low-charge Bi ions (which correlate with oxygen vacancies) through this present simple electroreduction method ($Bi^{3+} + xe^{−} \rightarrow Bi^{(3−x)+}$).[38,44] More importantly, most of oxygen vacancies (low-charge Bi ions) could be retained after being annealed in air/N_2 (1:1) atmosphere as the Bi $4f_{5/2}$ and Bi $4f_{7/2}$ peaks of AR-BiOI sample are slightly shifted to lower binding energy compared to the untreated BiOI sample. The bottom of Figure 2a compares the core-level Bi 4f XPS spectra of D-BiOI and AR-BiOI samples. Significantly, the Bi $4f_{5/2}$ and Bi $4f_{7/2}$
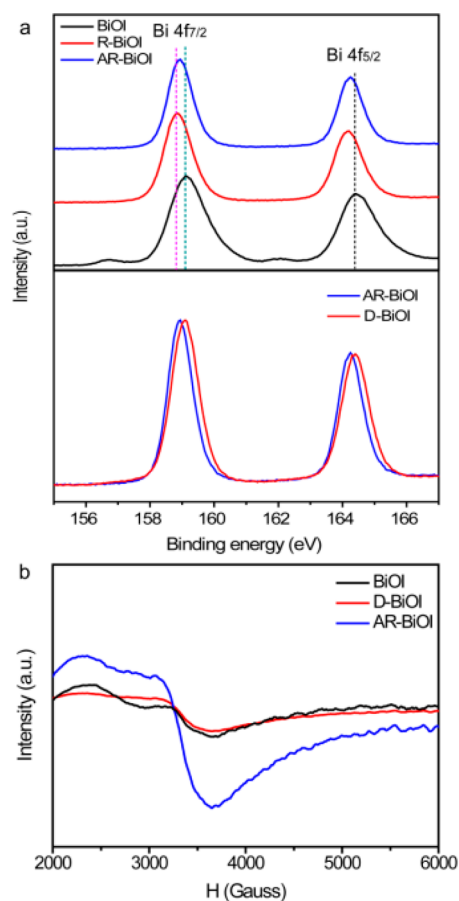
Figure 2. (a) Top: Normalized core-level Bi 4f XPS spectra collected for untreated BiOI (black), R-BiOI (red), and AR-BiOI (blue) samples. Bottom: Normalized core-level Bi 4f XPS spectra of D-BiOI and AR-BiOI samples. (b) EPR spectra of untreated BiOI, D-BiOI, and AR-BiOI samples collected at 77 K, where H is the magnetic field.

peaks of AR-BiOI sample are lower than those of D-BiOI sample, which confirms that the AR-BiOI sample has more low-charge Bi ions (oxygen vacancies) than the D-BiOI sample does.[38,44] More evidence can be observed from the electron spin resonance (EPR) spectra collected for the different BiOI samples. As shown in Figure 2b, all the BiOI samples exhibit an EPR signal at about $g = 2.0$, which is a typical signal of oxygen vacancies.[49]

To shed light on the correlation between oxygen vacancies and photocatalytic activity of BiOI nanosheets, we have studied the photocatalytic efficiencies of different BiOI samples on the degradation of MO under visible light irradiation ($\lambda > 420$ nm). Prior to the photocatalytic tests, all the BiOI samples with a film area of about 13.5 cm^2 (Supporting Information Figure S4) were magnetically stirred in the dark for 30 min to reach the adsorption–desorption equilibrium. The MO adsorption capabilities of all the BiOI samples were shown in Supporting Information Figure S5, and the pH value of the MO solution was 9. The MO adsorptions over untreated BiOI and D-BiOI samples are only 8.3% and 8.5%, while the AR-BiOI sample achieves 11.2%, revealing that the introduction of oxygen vacancies could slightly improve the adsorption capability of BiOI toward MO. Figure 3a shows the photodegradation efficiencies of MO as a function of irradiation time over different BiOI samples. The photolysis of MO by itself is negligible upon visible light irradiation under our experimental

conditions. Significantly, the AR-BiOI sample exhibited substantially higher efficiency than the untreated BiOI and D-BiOI samples. After 120 min of visible light irradiation, the MO degradations over P25, untreated BiOI, and D-BiOI samples are only 8.1%, 31.3%, and 48.8%, while the AR-BiOI sample achieves more than 99.1%. This result validly confirms our hypothesis that the introduction of oxygen vacancies could improve dramatically the photoactivity of BiOI for photocatalyst. The present efficiency of AR-BiOI nanosheets is also remarkably higher than the values of recently reported BiOI-based photocatalysts[18,20,33−36,49−52] (Supporting Information Table S1), such as BiOI/BiOCl,[33] BiOI/TiO$_2$,[36] BiOI/ZnO,[34] MnO$_x$−BiOI,[48] and ZnWO$_4$/BiOI.[35] Noteworthy is that the amount of the AR-BiOI sample used in our photocatalytic tests is much smaller (only 0.015 g for 100 mL of 10 g L$^{−1}$ MO solution) than these reported BiOI-based photocatalysts, further confirming the superior photocatalytic activity of our AR-BiOI sample. To verify the product of MO degradation, we used the saturated Ca(OH)$_2$ solution (Supporting Information Figure S6) to examine the product of degradation. Significantly, the clear saturated Ca(OH)$_2$ solution became turbid after dropping in 0.5 mL of the produced solution with light irradiation for 15 and 90 min. This result reveals that the MO was oxidized to CO$_2$ during light irradiation. Moreover, the products of degradation were also collected and analyzed by a total organic carbon analyzer.[53] From Supporting Information Table S2, the MO was decomposed into CO$_2$ under solar light irradiation.

Figure 3b compares the pseudo-first-order reaction kinetics of P25, untreated BiOI, D-BiOI, and AR-BiOI samples. The rate constant value of MO degradation for AR-BiOI sample is 0.033 min$^{−1}$, which is much higher than those of P25 (0.001 min$^{−1}$), untreated BiOI (0.003 min$^{−1}$), and D-BiOI (0.005 min$^{−1}$) samples, again showing the superior photocatalytic performance of the AR-BiOI sample. In addition, to confirm the stability of the high photocatalytic performance of the AR-BiOI nanosheets, recycling experiments for the photodegradation of MO were conducted. As depicted in Figure 3c, the AR-BiOI sample has excellent cycling stability with no any decay in its photocatalytic activity after five cycles. Furthermore, unlike the powder photocatalysts, the collection and recycle of AR-BiOI films are exceptionally simple and efficient, which only need to be directly taken out and washed by deionized water, and it does not bring new environmental pollution. Besides MO, the AR-BiOI sample also possesses excellent photocatalytic activities toward other dye pollutants such as methyl blue (MB), rhodamine B (RhB), Congo red (CR), acid orange II (AO II), phenol, etc. As shown in Figure 3d and Supporting Information Figure S7, the AR-BiOI sample could remove more than 96% of these dyes mentioned above after 120 min visible light irradiation. All these results convincingly demonstrate that the induced oxygen vacancies can effectively promote the photoactivity of BiOI.

For deep-seated insights into how oxygen vacancies affect the photocatalytic activity of BiOI nanosheets, we conducted the electrochemical impedance measurements, photoluminescence (PL) measurements, and photocurrent responses and recorded the UV−visible absorption spectra. Figure 4a shows the Mott−Schottky plots of the untreated BiOI, D-BiOI, and AR-BiOI samples, which were generated based on capacitances that were derived from the electrochemical impedance obtained at each potential at 10 kHz frequency. All the BiOI samples exhibited positive slopes in the Mott−Schottky plots, showing they are
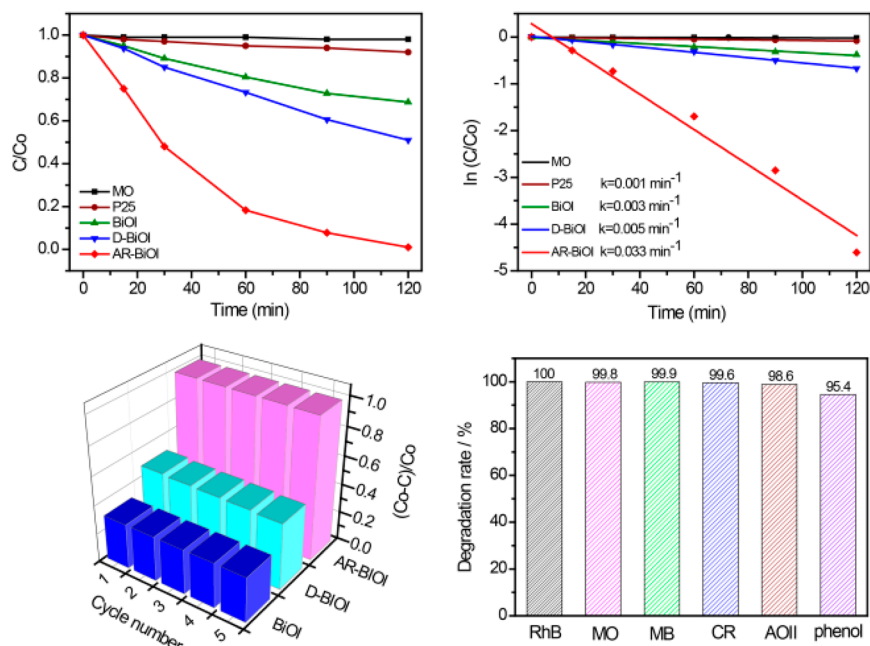
Figure 3. (a) Photocatalytic activity of untreated BiOI, D-BiOI, AR-BiOI, and P25 for degradation of MO under visible light irradiation. (b) Pseudo-first-order reaction kinetics of untreated BiOI, D-BiOI, AR-BiOI, and P25 samples. (c) Cycling performance of photocatalytic degradation of MO over untreated BiOI, D-BiOI, and AR-BiOI samples. (d) Photocatalytic activity of AR-BiOI for degradation of MO, RhB, MB, CR, AOII, and phenol after 120 min visible light irradiation.
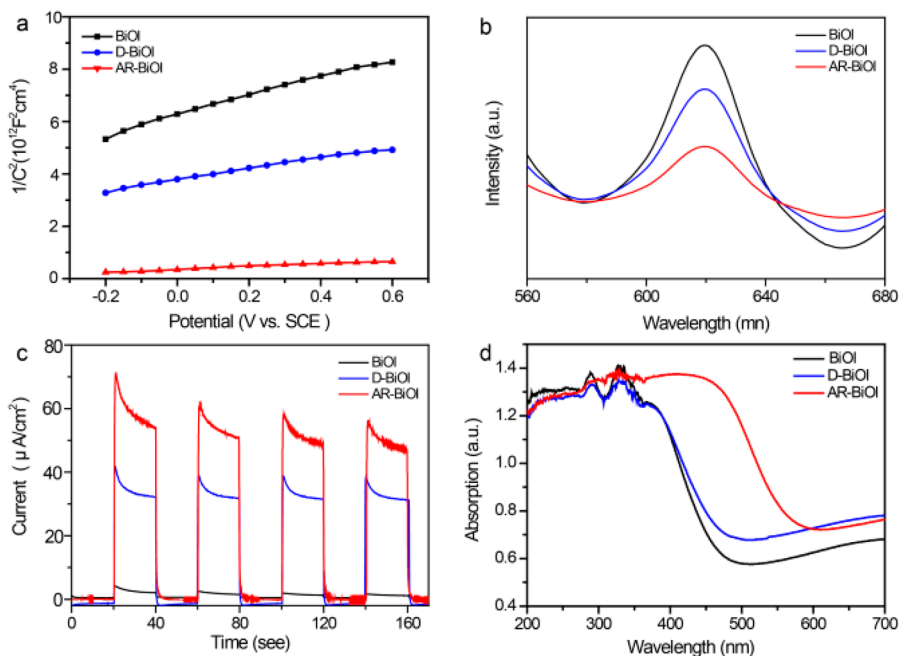

Figure 4. (a) Mott−Schottky plots of untreated BiOI, D-BiOI, and AR-BiOI samples obtained at each potential with 10 kHz frequency in the dark in a 0.1 M Na_2SO_4 electrolyte. (b) Photoluminescence spectra of untreated BiOI, D-BiOI, and AR-BiOI samples with an excitation wavelength of 400 nm. (c) Photocurrents responses of untreated BiOI, D-BiOI, and AR-BiOI samples under visible light irradiation. (d) UV−vis absorption spectra of untreated BiOI, D-BiOI, and AR-BiOI samples.

typical n-type semiconductors. The donor density of these n-type BiOI samples can be calculated from the slopes of Mott−Schottky plots using the following equation

$$N_d = (2/e_0 \varepsilon \varepsilon_0)[d(1/C^2)/dV]^{-1}$$

where N_d is the donor density, e_0 is the electron charge, ε is the dielectric constant of BiOI, ε_0 is the permittivity of vacuum, and V is the applied bias at the electrode. We could not calculate the

exact donor density of these BiOI samples due to the lack of the ε of BiOI. However, a qualitative comparison of donor densities between pristine BiOI, D-BiOI, and AR-BiOI electrodes using the slope of Mott−Schottky plots is reasonable, given that the donor density is inversely proportional to the slope of Mott−Schottky plots and they have similar morphology and specific surface area (15.1−15.6 m^2 g^{-1}, Supporting Information Figure S8). The fitting slopes of Mott−Schottky plots for pristine

BiOI, D-BiOI, and AR-BiOI samples are 3.6×10^{12}, 2.1×10^{12}, and 3.5×10^{11}, respectively. As expected, the AR-BiOI electrode exhibited substantially smaller slope compared to pristine BiOI and D-BiOI electrodes, confirming that the donor density of BiOI nanosheets was significantly increased after electroreduction and calcination. The remarkable enhancement in donor density is due to the increased amount of oxygen vacancies. The increased donor density can facilitate the separation and transport of photoexcited electrons, thereby suppressing the recommendation of the photogenerated carriers, which is further confirmed by photoluminescence (PL) spectra. As shown in Figure 4b, a strong emission band at ~620 nm was observed in pristine BiOI and D-BiOI nanosheets, which is attributed to the recombination of electron and hole.[54] However, the intensity of this emission peak for AR-BiOI sample was substantially low after inducing oxygen vacancy. The drastic quenching of the emission clear indicates the introduced oxygen vacancies can greatly facilitate the separation of photogenerated carriers of BiOI. Figure 4c compares the photocurrent response of these BiOI samples under visible light irradiation. Obviously, the photocurrent density of the AR-BiOI sample is much higher than those of the pristine BiOI and D-BiOI samples, revealing the superior visible-light-driven activity of the AR-BiOI nanosheets. All these results above reveal that the introduced oxygen vacancies serve as donor densities, which greatly improve the charge transportation and suppress the recommendation rate of the photogenerated electrons and holes, thus promoting the separation efficiency of the photogenerated carriers.[55]

Figure 4d shows the UV−visible absorption spectra of the untreated BiOI, D-BiOI, and AR-BiOI samples. The UV−visible absorption spectrum of the D-BiOI sample is similar to the untreated BiOI sample, suggesting that they have similar light absorption ability. Significantly, the absorption band edge of the AR-BiOI sample exhibited substantially red shift (about 103 nm) compared to the untreated BiOI and D-BiOI samples, revealing that the AR-BiOI sample could utilize more solar light. As an indirect semiconductor, the band gap of BiOI can be calculated from the plot of $(\alpha h \nu)^{1/2}$ versus photon energy $(h\nu)$.[14] From the Supporting Information Figure S9, the estimated band gap of AR-BiOI sample is about 1.61 eV, which is much smaller than those of untreated BiOI (1.87 eV) and D-BiOI (1.75 eV) samples. This convincingly supports that the introduction of oxygen vacancies can intrinsically improve the optical absorption property of BiOI. Therefore, based on the analyses above, the enhanced charge transportation and improved light-harvesting ability induced by oxygen vacancies are believed to be the major reasons for the superior photocatalytic activity of AR-BiOI.

To understand the nature of the primary active species involved in the photocatalytic degradation of MO over AR-BiOI sample under visible light irradiation, the photodegradation of MO was repeated with modification by adding 1 mmol of benzoquinone (BQ) as a superoxide radical scavenger ($^{\bullet}O^{2-}$) or 10 mmol of *tert*-butylalcohol (TBA) as a hydroxyl radical scavenger ($^{\bullet}OH$) or 10 mmol triethanolamine (TEOA) as a h^+ scavenger. As shown in Figure 5a, the removal efficiency of MO was obviously inhibited by TEOA, and the photodegradation of MO was only 34.5%, which was largely lower than in the absence of TEOA. The photodegradation of MO was inhibited slightly when BQ was added, while there was no obvious change with the addition of TBA. In addition, the photocatalytic activity of the AR-BiOI sample was greatly
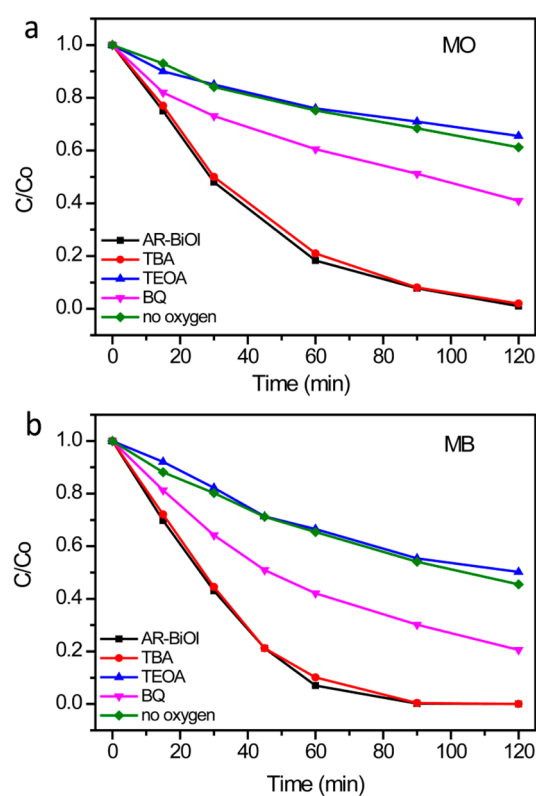

Figure 5. Effects of different scavengers on the degradation of MO (a) and MB (b) in the presence of AR-BiOI.

decreased without introducing O_2, showing that the presence of O_2 can further improve the photocatalytic performance of the AR-BiOI sample. This is due to fhe fact that the introduced O_2 could easily react with the photogenerated electron to produce active $^{\bullet}O^{2-}$ radicals, which can degrade the dye molecules. Similar results are also obtained from the photodegradation of MB (Supporting Information Figure S5b). Thus, it is believed that the degradation of dyes over AR-BiOI sample is dominated by the direct hole oxidation process and partly by the oxidation action of the generated $^{\bullet}O^{2-}$ radicals, rather than $^{\bullet}OH$ reactions taking place on the surface of the photocatalyst.

4. CONCLUSION

In summary, we have demonstrated that the introduction of oxygen vacancies improves significantly the photocatalytic performance of BiOI as visible-light-driven photocatalysts for dye degradation. Free-standing BiOI nanosheets with rich oxygen vacancies (AR-BiOI) that were obtained through fast-heating the electroreduced BiOI nanosheets exhibit substantially enhanced photocatalytic activity as compared to the untreated sample (BiOI) and the directly calcined sample (D-BiOI). The AR-BiOI nanosheets could eliminate more than 99.1% of MO within 120 min under visible light irradiation, which is considerably higher than those of untreated BiOI (31.3%) and D-BiOI (48.8%) samples at the same conditions. Additionally, the AR-BiOI nanosheets have an excellent cycling stability without any decrease of its photocatalytic activity after five cycles. Besides MO, the AR-BiOI nanosheets also possess prominent photocatalytic activities toward many dyes such as MB, RhB, CR, AO II, and phenol. Such enhanced photoactivity is believed to due to substantially increased visible light absorption and donor density as a result of formation of oxygen

vacancies. This work not only provides a new insight into the role of oxygen vacancies in promoting photocatalytic activity but also opens up new possibilities for efficient visible-light-driven photocatalysts.

■ ASSOCIATED CONTENT

Ⓢ Supporting Information

Synthetic details, experimental details, and additional descriptions, figures, and tables. This material is available free of charge via the Internet at http://pubs.acs.org.

■ AUTHOR INFORMATION

Corresponding Authors
*Phone: 86-20-84110071. Fax: 86-20-84112245. E-mail: luxh6@mail.sysu.edu.cn.
*Phone: 86-20-84110071. Fax: 86-20-84112245. E-mail: jihb@mail.sysu.edu.cn.

Author Contributions
The manuscript was written through contributions of all authors. All authors have given approval to the final version of the manuscript.

Notes
The authors declare no competing financial interest.

■ ACKNOWLEDGMENTS

■ REFERENCES

(1) Qu, Y.; Duan, X. Progress, Challenge and Perspective of Heterogeneous Photocatalysts. *Chem. Soc. Rev.* **2013**, *42*, 2568–2580.

(2) Weng, S.; Pei, Z.; Zheng, Z.; Hu, J.; Liu, P. Exciton-Free, Nonsensitized Degradation of 2-Naphthol by Facet-Dependent BiOCl under Visible Light: Novel Evidence of Surface-State Photocatalysis. *ACS Appl. Mater. Interfaces* **2013**, *5*, 12380–12386.

(3) Sun, Y.; Sun, Z.; Gao, S.; Cheng, H.; Liu, Q.; Lei, F.; Wei, S.; Xie, Y. All-Surface-Atomic-Metal Chalcogenide Sheets for High-Efficiency Visible-Light Photoelectrochemical Water Splitting. *Adv. Energy Mater.* **2014**, *4*, 1–11.

(4) Guerrero, M.; Altube, A.; García-Lecina, E.; Rossinyol, E.; Baró, M. D.; Pellicer, E.; Sort, J. Facile in Situ Synthesis of BiOCl Nanoplates Stacked to Highly Porous TiO₂: A Synergistic Combination for Environmental Remediation. *ACS Appl. Mater. Interfaces* **2014**, *6*, 13994–14000.

(5) Zhang, X.; Wang, X. B.; Wang, L. W.; Wang, W. K.; Long, L. L.; Li, W. W.; Yu, H. Q. Synthesis of a Highly Efficient BiOCl Single-Crystal Nanodisk Photocatalyst with Exposing (001) Facets. *ACS Appl. Mater. Interfaces* **2014**, *6*, 7766–7772.

(6) Weng, S.; Fang, Z.; Wang, Z.; Zheng, Z.; Feng, W.; Liu, P. Construction of Teethlike Homojunction BiOCl (001) Nanosheets by Selective Etching and Its High Photocatalytic Activity. *ACS Appl. Mater. Interfaces* **2014**, *6*, 18423–18428.

(7) Wang, G.; Wang, H.; Ling, Y.; Tang, Y.; Yang, X.; Fitzmorris, R. C.; Wang, C.; Zhang, J. Z.; Li, Y. Hydrogen-Treated TiO₂ Nanowire Arrays for Photoelectrochemical Water Splitting. *Nano Lett.* **2011**, *11*, 3026–3033.

(8) Pu, Y. C.; Wang, G.; Chang, K. D.; Ling, Y.; Lin, Y. K.; Fitzmorris, B. C.; Liu, C. M.; Lu, X.; Tong, Y.; Zhang, J. Z. Au Nanostructure-Decorated TiO₂ Nanowires Exhibiting Photoactivity Across Entire UV–Visible Region for Photoelectrochemical Water Splitting. *Nano Lett.* **2013**, *13*, 3817–3823.

(9) Wang, P.; Chen, P.; Kostka, A.; Marschall, R.; Wark, M. Control of Phase Coexistence in Calcium Tantalate Composite Photocatalysts for Highly Efficient Hydrogen Production. *Chem. Mater.* **2013**, *25*, 4739–4745.

(10) Qiu, Y.; Yan, K.; Deng, H.; Yang, S. Secondary Branching and Nitrogen Doping of ZnO Nanotetrapods: Building a Highly Active Network for Photoelectrochemical Water Splitting. *Nano Lett.* **2011**, *12*, 407–413.

(11) Wang, H.; Rogach, A. L. Hierarchical SnO₂ Nanostructures: Recent Advances in Design, Synthesis, and Applications. *Chem. Mater.* **2013**, *26*, 123–133.

(12) Qiu, Y.; Xu, G. L.; Kuang, Q.; Sun, S. G.; Yang, S. Hierarchical WO₃ Flowers Comprising Porous Single-Crystalline Nanoplates Show Enhanced Lithium Storage and Photocatalysis. *Nano Res.* **2012**, *5*, 826–832.

(13) Wang, G.; Ling, Y.; Wang, H.; Yang, X.; Wang, C.; Zhang, J. Z.; Li, Y. Hydrogen-Treated WO₃ Nanoflakes Show Enhanced Photostability. *Energy Environ. Sci.* **2012**, *5*, 6180–6187.

(14) Zhang, X.; Zhang, L. Electronic and Band Structure Tuning of Ternary Semiconductor Photocatalysts by Self Doping: The Case of BiOI. *J. Phys. Chem. C* **2010**, *114*, 18198–18206.

(15) Xiao, X.; Zhang, W. D. Facile Synthesis of Nanostructured BiOI Microspheres with High Visible Light-Induced Photocatalytic Activity. *J. Mater. Chem.* **2010**, *20*, 5866–5870.

(16) Lei, Y.; Wang, G.; Song, S.; Fan, W.; Pang, M.; Tang, J.; Zhang, H. Room Temperature, Template-Free Synthesis of BiOI Hierarchical Structures: Visible-Light Photocatalytic and Electrochemical Hydrogen Storage Properties. *Dalton Trans.* **2010**, *39*, 3273–3278.

(17) Cao, J.; Xu, B.; Luo, B.; Lin, H.; Chen, S. Novel BiOI/BiOBr Heterojunction Photocatalysts with Enhanced Visible Light Photocatalytic Properties. *Catal. Commun.* **2011**, *13*, 63–68.

(18) Liu, H.; Cao, W.; Su, Y.; Wang, Y.; Wang, X. Synthesis, Characterization and Photocatalytic Performance of Novel Visible-Light-Induced Ag/BiOI. *Appl. Catal., B* **2012**, *111*, 271–279.

(19) Liu, Q. C.; Ma, D. K.; Hu, Y. Y.; Zeng, Y. W.; Huang, S. M. Various Bismuth Oxyiodide Hierarchical Architectures: Alcohothermal-Controlled Synthesis, Photocatalytic Activities, and Adsorption Capabilities for Phosphate in Water. *ACS Appl. Mater. Interfaces* **2013**, *5*, 11927–11934.

(20) Cao, J.; Xu, B.; Lin, H.; Luo, B.; Chen, S. Novel Heterostructured Bi₂S₃/BiOI Photocatalyst: Facile Preparation, Characterization and Visible Light Photocatalytic Performance. *Dalton Trans.* **2012**, *41*, 11482–11490.

(21) Liao, C.; Ma, Z.; Dong, G.; Qiu, J. BiOI Nanosheets Decorated TiO₂ Nanofiber: Tailoring Water Purification Performance of Photocatalyst in Structural and Photo-Responsivity Aspects. *Appl. Surf. Sci.* **2014**, *314*, 481–489.

(22) Yang, J.; Xu, L.; Liu, C.; Xie, T. Preparation and Photocatalytic Activity of Porous Bi₅O₇I Nanosheets. *Appl. Surf. Sci.* **2014**, *319*, 265–271.

(23) Hu, J.; Weng, S.; Zheng, Z.; Pei, Z.; Huang, M.; Liu, P. Solvents Mediated-Synthesis of BiOI Photocatalysts with Tunable Morphologies and Their Visible-Light Driven Photocatalytic Performances in Removing of Arsenic From Water. *J. Hazard. Mater.* **2014**, *264*, 293–302.

(24) Mera, A. C.; Moreno, Y.; Pivan, J. Y.; Peña, O.; Mansilla, H. D. Solvothermal Synthesis of BiOI Microspheres: Effect of the Reaction Time on the Morphology and Photocatalytic Activity. *J. Photochem. Photobiol., A* **2014**, *289*, 7–13.

(25) Hahn, N. T.; Hoang, S.; Self, J. L.; Mullins, C. B. Spray Pyrolysis Deposition and Photoelectrochemical Properties of n-Type BiOI Nanoplatelet Thin Films. *ACS Nano* **2012**, *6*, 7712–7722.

(26) Su, J.; Xiao, Y.; Ren, M. Direct Hydrolysis Synthesis of BiOI Flowerlike Hierarchical Structures and Its Photocatalytic Activity under Simulated Sunlight Irradiation. *Catal. Commun.* **2014**, *45*, 30–33.

(27) He, R. a.; Cao, S.; Zhou, P.; Yu, J. Recent Advances in Visible Light Bi-Based Photocatalysts. *Chin. J. Catal.* **2014**, *35*, 989–1007.

(28) Niu, P.; Yin, L. C.; Yang, Y. Q.; Liu, G.; Cheng, H. M. Increasing the Visible Light Absorption of Graphitic Carbon Nitride (Melon) Photocatalysts by Homogeneous Self-Modification with Nitrogen Vacancies. *Adv. Mater.* **2014**, DOI: 10.1002/adma.201404057.

(29) Liu, G.; Wang, L.; Sun, C.; Yan, X.; Wang, X.; Chen, Z.; Smith, S. C.; Cheng, H. M.; Lu, G. Q. Band-to-Band Visible-Light Photon Excitation and Photoactivity Induced by Homogeneous Nitrogen Doping in Layered Titanates. *Chem. Mater.* **2009**, *21*, 1266−1274.

(30) Cheng, H.; Huang, B.; Dai, Y.; Qin, X.; Zhang, X. One-Step Synthesis of the Nanostructured AgI/BiOI Composites with Highly Enhanced Visible-Light Photocatalytic Performances. *Langmuir* **2010**, *26*, 6618−6624.

(31) Yu, C.; Yu, J. C.; Fan, C.; Wen, H.; Hu, S. Synthesis and Characterization of Pt/BiOI Nanoplate Catalyst with Enhanced Activity under Visible Light Irradiation. *Mater. Sci. Eng., B* **2010**, *166*, 213−219.

(32) Kim, W. J.; Pradhan, D.; Min, B. K.; Sohn, Y. Adsorption/ Photocatalytic Activity and Fundamental Natures of BiOCl and BiOCl$_x$I$_{1-x}$ Prepared in Water and Ethylene Glycol Environments, and Ag and Au-Doping Effects. *Appl. Catal., B* **2014**, *147*, 711−725.

(33) Li, T. B.; Chen, G.; Zhou, C.; Shen, Z. Y.; Jin, R. C.; Sun, J. X. New Photocatalyst BiOCl/BiOI Composites with Highly Enhanced Visible Light Photocatalytic Performances. *Dalton Trans.* **2011**, *40*, 6751−6758.

(34) Jiang, J.; Zhang, X.; Sun, P.; Zhang, L. ZnO/BiOI Heterostructures: Photoinduced Charge-Transfer Property and Enhanced Visible-Light Photocatalytic Activity. *J. Mater. Chem. C* **2011**, *115*, 20555−20564.

(35) Li, P.; Zhao, X.; Jia, C. j.; Sun, H.; Sun, L.; Cheng, X.; Liu, L.; Fan, W. ZnWO$_4$/BiOI Heterostructures with Highly Efficient Visible Light Photocatalytic Activity: The Case of Interface Lattice and Energy Level Match. *J. Mater. Chem. A* **2013**, *1*, 3421−3429.

(36) Dai, G.; Yu, J.; Liu, G. Synthesis and Enhanced Visible-Light Photoelectrocatalytic Activity of p−n Junction BiOI/TiO$_2$ Nanotube Arrays. *J. Phys. Chem. C* **2011**, *115*, 7339−7346.

(37) Lu, X.; Wang, G.; Zhai, T.; Yu, M.; Gan, J.; Tong, Y.; Li, Y. Hydrogenated TiO$_2$ Nanotube Arrays for Supercapacitors. *Nano Lett.* **2012**, *12*, 1690−1696.

(38) Wang, G.; Ling, Y.; Lu, X.; Qian, F.; Tong, Y.; Zhang, J. Z.; Lordi, V.; Rocha Leao, C.; Li, Y. Computational and Photo-electrochemical Study of Hydrogenated Bismuth Vanadate. *J. Phys. Chem. C* **2013**, *117*, 10957−10964.

(39) Lu, X.; Wang, G.; Xie, S.; Shi, J.; Li, W.; Tong, Y.; Li, Y. Efficient Photocatalytic Hydrogen Evolution over Hydrogenated ZnO Nanorod Arrays. *Chem. Commun.* **2012**, *48*, 7717−7719.

(40) Zhang, X.; Zhao, L.; Fan, C.; Liang, Z.; Han, P. Effects of Oxygen Vacancy on the Electronic Structure and Absorption Spectra of Bismuth Oxychloride. *Comput. Mater. Sci.* **2012**, *61*, 180−184.

(41) Chen, X.; Liu, L.; Peter, Y. Y.; Mao, S. S. Increasing Solar Absorption for Photocatalysis with Black Hydrogenated Titanium Dioxide Nanocrystals. *Science* **2011**, *331*, 746−750.

(42) Etacheri, V.; Seery, M. K.; Hinder, S. J.; Pillai, S. C. Oxygen Rich Titania: A Dopant Free, High Temperature Stable, and Visible-Light Active Anatase Photocatalyst. *Adv. Funct. Mater.* **2011**, *21*, 3744−3752.

(43) Xie, K.; Umezawa, N.; Zhang, N.; Reunchan, P.; Zhang, Y.; Ye, J. Self-Doped SrTiO$_3$ Photocatalyst with Enhanced Activity for Artificial Photosynthesis under Visible Light. *Energy Environ. Sci.* **2011**, *4*, 4211−4219.

(44) Ye, L.; Deng, K.; Xu, F.; Tian, L.; Peng, T.; Zan, L. Increasing Visible-Light Absorption for Photocatalysis with Black BiOCl. *Phys. Chem. Chem. Phys.* **2012**, *14*, 82−85.

(45) Huang, W. L. Electronic Structures and Optical Properties of BiOX (X = F, Cl, Br, I) via DFT Calculations. *J. Comput. Chem.* **2009**, *30*, 1882−1891.

(46) Huang, W. L. Electronic Structures and Optical Properties of BiOX (X = F, Cl, Br, I) via DFT Calculations. *Comput. Mater. Sci.* **2012**, *55*, 166−170.

(47) Mu, Q.; Zhang, Q.; Wang, H.; Li, Y. Facile Growth of Vertically Aligned BiOCl Nanosheet Arrays on Conductive Glass Substrate with High Photocatalytic Properties. *J. Mater. Chem.* **2012**, *22*, 16851−16857.

(48) Ye, L.; Liu, X.; Zhao, Q.; Xie, H.; Zan, L. Dramatic Visible Light Photocatalytic Activity of MnOx−BiOI Heterogeneous Photocatalysts and the Selectivity of the Cocatalyst. *J. Mater. Chem. A* **2013**, *1*, 8978−8983.

(49) Jiang, J.; Zhang, L.; Li, H.; He, W.; Yin, J. J. Self-Doping and Surface Plasmon Modification Induced Visible Light Photocatalysis of BiOCl. *Nanoscale* **2013**, *5*, 10573−10581.

(50) Wang, Y.; Deng, K.; Zhang, L. Visible Light Photocatalysis of BiOI and Its Photocatalytic Activity Enhancement by in Situ Ionic Liquid Modification. *J. Phys. Chem. C* **2011**, *115*, 14300−14308.

(51) Lin, H.; Ye, H.; Li, X.; Cao, J.; Chen, S. Facile Anion-Exchange Synthesis of BiOI/BiOBr Composite with Enhanced Photoelectro-chemical and Photocatalytic Properties. *Ceram. Int.* **2014**, *7*, 9743−9750.

(52) Cao, J.; Zhou, C.; Lin, H.; Xu, B.; Chen, S. Direct Hydrolysis Preparation of Plate-Like BiOI and Their Visible Light Photocatalytic Activity for Contaminant Removal. *Mater. Lett.* **2013**, *109*, 74−77.

(53) Xie, S.; Zhai, T.; Li, W.; Yu, M.; Liang, C.; Gan, J.; Lu, X.; Tong, Y. Hydrogen Production from Solar Driven Gucose Oxidation over Ni(OH)$_2$ Functionalized Electroreduced TiO$_2$ Nanowire Arrays. *Green Chem.* **2013**, *15*, 2434−2440.

(54) Yu, C.; Yu, J. C.; Fan, C.; Wen, H.; Hu, S. Synthesis and Characterization of Pt/BiOI Nanoplate Catalyst with Enhanced Activity under Visible Light Irradiation. *Mater. Sci. Eng., B* **2010**, *166*, 213−219.

(55) Jiang, X.; Zhang, Y.; Jiang, J.; Rong, Y.; Wang, Y.; Wu, Y.; Pan, C. Characterization of Oxygen Vacancy Associates within Hydro-genated TiO$_2$: A Positron Annihilation Study. *J. Phys. Chem. C* **2012**, *116*, 22619−22624.